fluids

MDPI

Article

Bubble Growth in Supersaturated Liquids

Raj Kumar Nayak Maloth, Roger E. Khayat * and Christopher T. DeGroot

Department of Mechanical and Material Engineering, University of Western Ontario, London, ON N6A 3K7, Canada
* Correspondence: rkhayat@uwo.ca

Abstract: Bubble formation and dissolution have a wide range of industrial applications, from the production of beverages to foam manufacturing processes. The rate at which the bubble expands or contracts has a significant effect on these processes. In the current work, the hydrodynamics of an isolated bubble expanding due to mass transfer in a pool of supersaturated gas–liquid solution is investigated. The complete scalar transportation equation (advection–diffusion) is solved numerically. It is observed that the present model accurately predicted bubble growth when compared with existing approximated models and experiments. The effect of gas–liquid solution parameters such as inertia, viscosity, surface tension, diffusion coefficient, system pressure, and solubility of the gas has been investigated. It is found that the surface tension and inertia have a very minimal effect during the bubble expansion. However, it is observed that the viscosity, system pressure, diffusion, and solubility have a considerable effect on bubble growth.

Keywords: bubble growth; hydrodynamics; supersaturated liquids; 1-d moving interface; advection–diffusion process

check for updates

Citation: Maloth, R.K.N.; Khayat, R.E.; DeGroot, C.T. Bubble Growth in Supersaturated Liquids. *Fluids* **2022**, *7*, 365. https://doi.org/10.3390/fluids7120365

Academic Editor: Mehrdad Massoudi

Received: 18 October 2022
Accepted: 22 November 2022
Published: 25 November 2022

Publisher's Note: MDPI stays neutral with regard to jurisdictional claims in published maps and institutional affiliations.

Copyright: © 2022 by the authors. Licensee MDPI, Basel, Switzerland. This article is an open access article distributed under the terms and conditions of the Creative Commons Attribution (CC BY) license (https://creativecommons.org/licenses/by/4.0/).

1. Introduction

A gas bubble is formed when an atomically or molecularly dissolved gas becomes supersaturated in a liquid solvent as a result of the reduction in imposed gas pressure, change in liquid temperature, or change in solute or solvent character Rosner et al., 1972, [1]. The study of gas bubbles is of major interest due to their appearance in many real-world problems. One of the important applications of bubble hydrodynamics is in chemical process industries, for example in the production of foamed plastics Elshereef et al., 2010, [2]. When a gas-generating substance such as a blowing agent is mixed with a high-pressure molten polymer, the resulting product turns out to be thermoplastic Arefmanesh et al., 1992, [3]. In this process, gas bubbles emerge and have a considerable effect on product quality. Therefore, it is necessary to understand the behavior of bubbles under different process parameter conditions. High-density foamed thermoplastics, otherwise called cellular plastics, are used in household furniture, transportation, and building products; on the other hand, low-density thermoplastics are frequently used in rigid packing Lee et al., 1996, [4]. The formation and growth of bubbles due to de-gassing or reduction in pressure in a supersaturated gas–liquid solution is observed in a broader spectrum of industrial and natural processes. For example, a very well-known process in which de-gassing is observed are carbonated beverages, such as beer, soda, and champagne (Bisperink et al., 1994, [5]; Jones et al., 1999, [6]; Barker et al., 2002, [7]; Liger-Belair 2005, [8]; Lee et al., 2011, [9]; Enríquez et al., 2013, [10] Enríquez et al., 2014, [11]). The study of bubble dynamics is vital in production industries, where molten polymers, metals, and glasses are of major interest Amon and Denson, 1984, [12] and a bubble prediction theory is important in the exsolution of gases during oil extraction Pooladi-Darvish et al., 1999, [13].

Several mathematical models have been developed to predict the bubble size evolution in various industrial processes. For instance, Epstein and Plesset, 1950, [14] derived

an approximate analytical solution, by neglecting inertia, to an unbounded single bubble growth/dissolution in a gas–liquid solution due to pure mass transfer (diffusion) for supersaturated and undersaturated conditions. Epstein's formulation suggests that the bubble grows as the square root of time, i.e., $\overline{R} \propto \sqrt{\overline{t}}$, where $\overline{R}$ is the radius of the bubble. However, their formulation lacks in explaining the hydrodynamic effects on bubble growth, including inertia, surface tension, etc. Barlow and Langlois, 1962, [15] were the first to combine diffusion with hydrodynamics, wherein they introduced a very complicated integro-differential equation based on a thin shell assumption. The formulation of Barlow et al. is complicated and computationally time-consuming to solve for larger bubble growth rates. Rosner and Epstein, 1972, [1] assumed a parabolic concentration profile in a thin boundary layer to generate an approximate solution of the diffusion equation. This work has been adopted by many researchers including Elshereef et al., 2010, [2], Patel, 1980, [16] and Han and Yoo, 1981, [17] formulation does not account for the change in gas pressure inside the bubble with time. Patel, 1980, [16] developed two coupled ordinary differential equations (ODEs) for predicting the unbounded growth of a single bubble in a Newtonian liquid; however, he neglected the effect of inertia in his formulation. Later, Amon and Denson, 1984, [12] introduced a cell-based model that incorporates the effect of available gas from the surrounding bubbles. Amon and Denson's formulation is developed based on a cell model assumption, where they have considered the foam as a summation of an equal microscopic unit of spherical cells with a constant mass in it and every cell has a spherical gas bubble that grows by diffusion of gas from the microscopic unit.

As discussed earlier, Barlow et al., 1962, [15] and Patel, 1980, [16] developed models for pure Newtonian fluid cases, hence neglected the effect of the elastic nature of the polymer. To fill this gap, Han and Yoo, 1981, [17] and Ramesh et al., 1991, [18] introduced a model that includes the effect of the elasticity of the fluid (polymer). Elshereef et al., 2010, [2] compared two popular bubble growth models. The first model is known as the Patel model or single bubble growth model, which is developed on assumption that a single bubble grows in a pool of liquid with infinite availability of gas, and the second model is called a cell model or Amon and Denson model, which is developed by incorporating the finiteness of gas availability and considering the proximity of gas bubbles. The main motivation of the Elshereef et al., 2010, [2] investigation was to compare these two models in terms of numerical implementations and accuracy in bubble growth prediction. In this regard, they compared the models with Han and Yoo's experimental findings. In recent years, Soto et al., 2019, 2020, [19,20] investigated experimentally carbon dioxide (CO_2) and nitrogen (N_2) bubble growth in water solutions with and without confinements. Their finding suggests that after the initial period of diffusion-driven bubble growth, the mass transfer is further accelerated due to density-driven convective flow.

Although researchers have performed ample work in understanding the hydrodynamics of the bubbles in different processes, clear insight into the diffusion process coupling with hydrodynamics and an explanation of process flow parameters' effects on hydrodynamics are lacking. The current work emphasizes solving the diffusion process numerically and closely studying how different liquid parameters such as liquid viscosity, surface tension, diffusion coefficient, system pressure, and solubility of gas affect the hydrodynamics of bubble growth. Though the current numerical framework developed in this work is for Newtonian liquids, the authors aim to explore how the current model compares with the different Newtonian liquid models of Elshereef et al., 2010, [2] and the viscoelastic experimental data of Han and Yoo, 1981, [17].

2. Physical Domain and Problem Formulation

2.1. The Physical Domain

The hydrodynamics of an isolated, spherically symmetrical gas bubble of radius $\overline{R}(\overline{t})$, where $\overline{t}$ is the time, in an incompressible gas–liquid solution is examined in spherical coordinates $(\overline{r}, \overline{\theta}, \overline{\phi})$. Barred variables denote dimensional quantities. We assume a stationary single bubble of initial radius $\overline{R}_0$ and a gas pressure $\overline{p}_{g0}$ nucleating in a saturated solution

of gas and liquid with the partial pressure of the gas in the liquid $\overline{p}_0$ and concentration $\overline{c}_0$, as shown in Figure 1. Denoting the interfacial tension by σ, then $\overline{p}_{g0} = \frac{\sigma}{\overline{R}_0} + \overline{p}_0$. At $\overline{t} = 0^+$, the gas–liquid solution is suddenly exposed to a drop in pressure when the atmospheric pressure $\overline{p}_a$ is applied in the bulk liquid region far from the gas bubble, and where it is assumed maintained for all time $\overline{t} > 0$. We denote by $\overline{p}_R(\overline{t})$ the pressure at the gas–liquid interface and by $\overline{p}_g(\overline{t})$, the gas pressure inside the bubble. The concentration of the gas in the liquid at a given time and position is denoted by $\overline{c}(\overline{r}, \overline{t})$, whereas the concentration at the interface of the bubble is $\overline{c}_R(\overline{t}) \equiv \overline{c}(\overline{r} = \overline{R}, \overline{t})$. Due to the spherical symmetry assumption the velocity components $\overline{v}$ and $\overline{w}$ in the direction $\overline{\theta}$ *and* $\overline{\phi}$ vanishes. Therefore, the only non-vanishing liquid velocity component is in radial direction and denoted by $\overline{u}(\overline{r}, \overline{t})$ and the bubble interface velocity is given by $\frac{d\overline{R}}{d\overline{t}} = \overline{u}(\overline{r} = \overline{R}, \overline{t})$ Maloth, 2020, [21]. Henry's law is assumed to apply initially so that $\overline{c}_0 = k_H \overline{p}_0$ and at the interface so that $\overline{c}_R(\overline{t}) = k_H \overline{p}_R(\overline{t})$, where k_H is Henry's constant. Finally, as it is customarily done in the literature, we assume that the concentration far from the bubble retains its initial level as it is not affected by the sudden drop in pressure during the transient process of bubble growth. Thus, $\overline{c}(\overline{r} \to \infty, \overline{t}) \sim \overline{c}_0$.

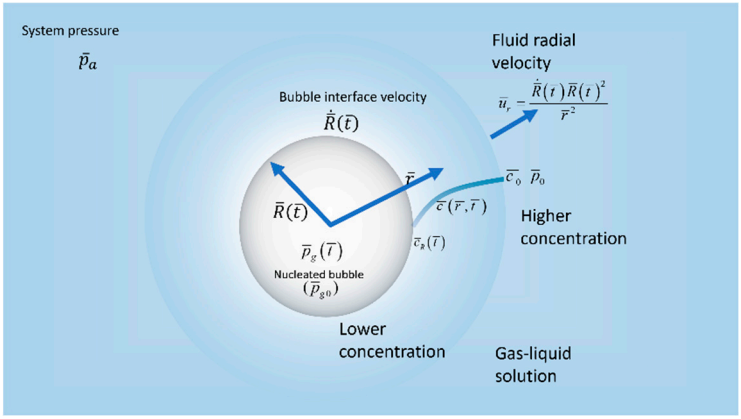


Figure 1. Schematic diagram of a single bubble in a liquid–gas solution.

2.2. Conservation of Mass and Linear Momentum

The flow of the Newtonian liquid of density ρ_L and viscosity μ_L is assumed to be spherically symmetric, thus reducing to a transient one-dimensional problem in the radial direction, $\overline{r}$. The conservation of mass and momentum in the liquid region reduces to

$$\frac{\partial \overline{u}}{\partial \overline{r}} + 2\frac{\overline{u}}{\overline{r}} = 0 \tag{1}$$

$$\rho_L\left(\frac{\partial \overline{u}}{\partial \overline{t}} + \overline{u}\frac{\partial \overline{u}}{\partial \overline{r}}\right) = -\frac{\partial \overline{p}}{\partial \overline{r}} + 2\mu_L\left(\frac{\partial^2 \overline{u}}{\partial \overline{r}^2} + \frac{1}{\overline{r}}\frac{\partial \overline{u}}{\partial \overline{r}} - \frac{1}{\overline{r}^2}\overline{u}\right). \tag{2}$$

These equations are subject to the following initial and boundary conditions. Initially, the bubble is assumed to be of radius $\overline{R}_0$ and at rest, so that

$$\overline{R}(t = 0) = \overline{R}_0,\ \overline{u}(\overline{r}, \overline{t} = 0) = 0. \tag{3}$$

The kinematic and dynamic boundary conditions at the interface take the form:

$$\overline{u}(\overline{r} = \overline{R}, \overline{t}) = \frac{d\overline{R}}{d\overline{t}} \tag{4}$$

$$\overline{p}_g(\overline{t}) = 2\frac{\sigma}{\overline{R}(\overline{t})} + \overline{p}(\overline{r} = \overline{R}, \overline{t}) + 4\frac{\mu_L}{\overline{R}(\overline{t})}\overline{u}(\overline{r} = \overline{R}, \overline{t}), \tag{5}$$

where σ is the interfacial tension. In stating condition (5), the gas inside the bubble is assumed to be motionless. Integrating Equation (1) and using condition (4) leads to

$$\overline{u}(\overline{r},\overline{t}) = \frac{\overline{R}^2}{\overline{r}^2}\frac{d\overline{R}}{d\overline{t}}. \tag{6}$$

Substituting this expression for the radial velocity and integrating Equation (2) over the interval $\overline{r} \in (\overline{R}, \infty)$, and eliminating the pressure at the interface from conditions (5) yields the Rayleigh–Plesset equation:

$$\rho_L\left[\overline{R}\frac{d^2\overline{R}}{d\overline{t}^2} + \frac{3}{2}\left(\frac{d\overline{R}}{d\overline{t}}\right)^2\right] = \overline{p}_g(\overline{t}) - 2\frac{\sigma}{\overline{R}} - 4\frac{\mu_L}{\overline{R}}\frac{d\overline{R}}{d\overline{t}} - \overline{p}_a. \tag{7}$$

Here, the growth of the bubble is dictated by the pressure difference $\overline{p}_g - \overline{p}_a$, where $\overline{p}_g > \overline{p}_a$. We note that the pressure at infinity is the surrounding or ambient pressure of the liquid and is equal to $\overline{p}_a$. Equation (7) can be solved once and $\overline{p}_g(\overline{t})$ is determined. The evolution of the gas pressure inside the bubble is directly related to the evolution and distribution of the gas concentration in the liquid, which is formulated next.

2.3. Concentration and Mass Transfer

In a supersaturated liquid, bubbles grow due to the diffusion of mass across the interface. Therefore, the diffusive mass flux across the interface is equal to the rate of change in mass inside the gas bubble. According to Fick's first law, the time rate of change in mass flux $\dot{m}_R$ at the interface of the spherical bubble is then given by

$$\frac{d\overline{m}_R}{d\overline{t}} = 4\pi\overline{R}^2 D\left(\frac{\partial\overline{c}}{\partial\overline{r}}\right)_{\overline{R}}. \tag{8}$$

Here, $\left(\frac{\partial\overline{c}}{\partial\overline{r}}\right)_{\overline{R}} = \frac{\partial\overline{c}}{\partial\overline{r}}(\overline{r}=\overline{R},\overline{t})$ is the concentration gradient of the gas at the interface and D (m^2/s) is the diffusion coefficient of the gas–liquid solution. Now, let the mass of the gas inside the bubble be $\overline{m}_g(\overline{t}) = \frac{4}{3}\pi\overline{\rho}_{g0}(\overline{t})\overline{R}^3(\overline{t})$, where $\overline{\rho}_g(\overline{t})$ is the gas density. Then, the rate of change in mass inside the spherical bubble is

$$\frac{d\overline{m}_g}{d\overline{t}} = 4\pi\overline{R}^2\left(\overline{\rho}_g\dot{\overline{R}} + \frac{\overline{R}}{3}\overline{\rho}_g\right). \tag{9}$$

Assuming that the gas inside the bubble follows the ideal gas law, the density of the gas can be eliminated in terms of the pressure as $\overline{\rho}_g(\overline{t}) = \frac{\overline{p}_g(\overline{t})M}{R_g\overline{T}_g}$, where R_g is the universal gas constant; $\overline{T}_g$ is the temperature of the gas, which is assumed to remain constant throughout the transient process; and M is the molar gas weight. We also assume that, after nucleation, the pressure inside the bubble is in equilibrium with the initial saturation pressure $\overline{p}_{g0}$ and density $\overline{\rho}_{g0}$. In this case, we can write $\overline{\rho}_g(\overline{t}) = \frac{\overline{\rho}_{g0}}{\overline{p}_{g0}}\overline{p}_g(\overline{t})$, and Equation (9) becomes

$$\frac{d\overline{m}_g}{d\overline{t}} = 4\pi\frac{\overline{\rho}_{g0}}{\overline{p}_{g0}}\overline{R}^2\left(\overline{p}_g\frac{d\overline{R}}{d\overline{t}} + \frac{\overline{R}}{3}\frac{d\overline{p}_g}{d\overline{t}}\right) \tag{10}$$

Upon introducing (10) into Equation (8), we obtain the desired equation for the pressure inside the gas bubble:

$$\frac{d\overline{p}_g}{d\overline{t}} = 3\frac{\overline{p}_{g0}}{\overline{\rho}_{g0}}D\frac{1}{\overline{R}}\left(\frac{\partial\overline{c}}{\partial\overline{r}}\right)_{\overline{R}} - 3\frac{\overline{p}_g}{\overline{R}}\frac{d\overline{R}}{d\overline{t}}. \tag{11}$$

This is the pressure equation resulting from the thermodynamic equilibrium at the interface. This first-order equation requires one initial condition on the pressure inside the bubble, which is formally written as

$$\overline{p}_g(\overline{t}=0)=\overline{p}_{g0}. \tag{12}$$

Equations (7) and (11) reflect the coupling between the bubble growth and pressure evolution inside the bubble. The presence of the concentration gradient at the interface in (11) also signals an additional coupling with the gas concentration across the saturated liquid, which is governed by an advection–diffusion equation, as shown next.

The concentration of gas in the liquid $\overline{c}(\overline{r},\overline{t})$ can be described by the scalar transport advection–diffusion equation which, when the velocity is substituted from (6) in the convective term, becomes

$$\frac{\partial\overline{c}}{\partial\overline{t}}+\frac{\overline{R}^2}{\overline{r}^2}\frac{d\overline{R}}{d\overline{t}}\frac{\partial\overline{c}}{\partial\overline{r}}=D\left(\frac{2}{\overline{r}}\frac{\partial\overline{c}}{\partial\overline{r}}+\frac{\partial^2\overline{c}}{\partial\overline{r}^2}\right). \tag{13}$$

The initial condition for Equation (13) comes from the assumption that, after the nucleation of the bubble, the concentration is uniformly distributed in the liquid, and it is equal to the dissolved concentration $\overline{c}_0$. Therefore, it is written as

$$\overline{c}(\overline{r},\overline{t}=0)=\overline{c}_0. \tag{14}$$

The remaining two boundary conditions for Equation (13) are the equilibrium condition of the concentration at the interface, which is described by Henry's law,

$$\overline{c}(\overline{r}=\overline{R},\overline{t})=\overline{c}_R(\overline{t})=k_H\overline{p}_g(\overline{t}), \tag{15}$$

where k_H is Henry's constant. The concentration far from the bubble is assumed to be equal to the saturation concentration:

$$\overline{c}(\overline{r}\to\infty,\overline{\mathrm{t}})\sim\overline{c}_0=k_H\overline{p}_0=k_H\left(\overline{p}_{g0}-2\frac{\sigma}{\overline{R}_0}\right). \tag{16}$$

This completes the formulation of the problem, which illustrates the non-linear coupling among the bubble growth, gas pressure, and concentration in the liquid region.

Equation (11) is similar to the pressure formulation of Elshereef et al., 2010, [2]. However, they assumed an approximate analytical solution to calculate the concentration gradient that appears in Equation (11). In the present work, one of the main goals is to solve the fully coupled problem numerically using a finite difference approach and compare it with the approximated analytical results.

3. Non-Dimensionalization and Solution Procedure

3.1. The Dimensionless Problem

The equations and their initial and boundary conditions are non-dimensionalized as follows. The velocity scale is taken as $\overline{V}=\sqrt{\frac{(\overline{p}_{g0}-\overline{p}_a)}{\rho_L}}$, which is related to the initial driving pressure difference, the length scale is the initial bubble radius $\overline{R}_0$, the pressure scale is the initial gas pressure $\overline{p}_{g0}$, and the concentration scale is the equilibrium concentration $\overline{c}_0$. In this case, the time scale is naturally $\frac{\overline{R}_0}{\overline{V}}$. The dimensionless variables become

$$r=\frac{\overline{r}}{\overline{R}_0},\ c=\frac{\overline{c}}{\overline{c}_0},\ t=\frac{\overline{V}}{\overline{R}_0}\overline{t},\ R=\frac{\overline{R}}{\overline{R}_0},\ p=\frac{\overline{p}}{\overline{p}_{g0}}\,. \tag{17}$$

There are five non-dimensional groups appearing in the problem, three familiar groups: the Reynolds number Re, the capillary number Ca and the Péclet number Pe. More explicitly:

$$Re = \frac{\rho_L \overline{V}\, \overline{R}_0}{\mu_L}, \tag{18a}$$

$$Ca = \frac{\rho_L \overline{V}^2 \overline{R}_0}{\sigma} = \frac{(\overline{p}_{g0} - \overline{p}_a)\overline{R}_0}{\sigma}, \tag{18b}$$

$$Pe = \frac{\overline{V}\, \overline{R}_0}{D}. \tag{18c}$$

Here, the Reynolds number (Re) compares the inertial force due to bubble growth in the liquid region with the liquid viscosity. The capillary number (Ca) weighs between viscous forces from the liquid to the surface tension forces at the interface of the bubble and the liquid and the Péclet number describes the ratio between the convection mass transfer to the diffusive mass transfer of gas from the liquid into the bubble.

The additional two new non-dimensional parameters are denoted by P and C, the former being the ratio of the initial pressure to the pressure difference, and the latter reflects the initial level of gas solubility:

$$P = \frac{\overline{p}_{g0}}{\overline{p}_{g0} - \overline{p}_a} = \frac{1}{1 - p_a}, \tag{19a}$$

$$C = \frac{\overline{c}_0}{\overline{\rho}_{g0}}. \tag{19b}$$

Finally, a sixth additional parameter in the problem is the dimensionless atmospheric-to-gas pressure ratio $p_a = \frac{\overline{p}_a}{\overline{p}_{g0}}$.

3.2. Domain Mapping

The interface of the bubble changes with time, which makes the numerical procedure for solving the concentration distribution in the liquid more complicated and time-consuming. We implement an implicit finite difference in space and integrate the resulting equations with respect to time. One obvious but costly approach is to track the interface of the bubble with time and re-mesh the computational domain at each time step.

Alternatively, we recast the concentration Equation (13) in terms of Lagrangian coordinates $\overline{x}(\overline{r}, \overline{t}) = \overline{r} - \overline{R}(t)$, such that at all time intervals the interface is fixed. Therefore, after non-dimensionalization and coordinate transformation the Equations (7), (11) and (13) takes the form:

$$R\frac{d^2R}{dt^2} + \frac{3}{2}\left(\frac{dR}{dt}\right)^2 = P(p_g - p_a) - \frac{2}{CaR} - \frac{4}{ReR}\frac{dR}{dt}. \tag{20}$$

$$\frac{dp_g}{dt} = 3\frac{C}{RPe}\left(\frac{\partial c}{\partial x}\right)_{x=0} - 3\frac{p_g}{R}\frac{dR}{dt} \tag{21}$$

$$\frac{\partial c}{\partial t} + \frac{\partial c}{\partial x}\left(\frac{\dot{R}R^2}{(x+R)^2} - \dot{R}\right) = \frac{1}{Pe}\left(\frac{2}{x+R}\frac{\partial c}{\partial x} + \frac{\partial^2 c}{\partial x^2}\right) \tag{22}$$

The rescaled initial and boundary conditions are deduced from (3), (12), and (14) to:

$$R(t=0) = 1, \tag{23a}$$

$$\dot{R}(t=0) = 0, \tag{23b}$$

$$p_g(t=0) = 1, \tag{23c}$$

$$c(x, t = 0) = 1. \tag{23d}$$

$$c(x = 0, t) = p_g(t), \tag{24a}$$

$$c(\, x \to \infty, t\,) = 1. \tag{24b}$$

3.3. Numerical Implementation

Equation (20) is a non-linear, second-order ODE that describes the bubble growth. If the pressure in the bubble is constant, Equation (20) can be solved for the bubble growth $R(t)$ and its interface velocity $\dot{R}(t)$ with the use of any readily available numerical time integration solver, such as ode45 in MathWorks MATLAB version R2019b. However, the difficulty arises when the pressure inside the bubble varies with time, and it then needs to be coupled with the scalar diffusion equation to solve for the concentration gradient at the interface. Additionally, the scalar diffusion Equation (22) contains a highly non-linear convective term in terms of bubble radius and interface velocity. This combination makes the equations stiffer and involves solving Equations (20)–(22) simultaneously. Therefore, solving the highly stiff equations with ode45 takes a tremendous amount of time. Instead of ode45, a variable order of accuracy solver, ode15s, is used to integrate the equations. Here, ode15s uses first to fifth orders, changing the order as required. This solver takes much less time compared to the ode45 solver without compromising accuracy.

To solve these two equations simultaneously, the second-order non-linear hydrodynamic Equation (20) primarily needs to be converted into the system of first-order ODEs by letting $R = y_1$. Therefore, the system of first-order ODEs is given as

$$\frac{dR}{dt} = y_2 \tag{25}$$

$$\frac{dy_2}{dt} = \frac{1}{y_1}\left(P(p_g - p_a) - \frac{2}{y_1 Ca} - \frac{4y_2}{y_1 Re} - \frac{3}{2}y_2^2\right) \tag{26}$$

This way, when Equation (25) is integrated, one can obtain y_2, which is bubble interface velocity, and similarly Equation (26) is integrated to obtain y_1, which is the bubble radius. Since Equation (26) includes partial derivates in time and space, one can approximate either time or space using the finite difference methods. For convenience, the space partial derivative is approximated with a finite difference, up to second-order accuracy.

Let i be the node position and N be the total number of nodes (see Figure 2) in the gas–liquid solution, starting from the interface x = 0 to infinity. The central difference scheme is adopted for the derivates. Therefore, the finite difference approximation for the first- and second-order derivatives with central difference schemes are written as

$$\frac{\partial c}{\partial x} = \frac{c_{i+1} - c_{i-1}}{2dx} \tag{27}$$

$$\frac{\partial^2 c}{\partial x^2} = \frac{c_{i+1} - 2c_i + c_{i-1}}{dx^2} \tag{28}$$

The discretized form of the scalar diffusion equation using Equations (27) and (28) takes the form

$$\frac{dc_i}{dt} = \frac{1}{Pe}\left(\frac{2}{(x_i + R)}\left(\frac{c_{i+1} - c_{i-1}}{2dx}\right) + \left(\frac{c_{i+1} - 2c_i + c_{i-1}}{dx^2}\right)\right) - \left(\frac{c_{i+1} - c_{i-1}}{2dx}\right)\left(\frac{\dot{R}R^2}{(x_i + R)^2} - \dot{R}\right) \tag{29}$$

The discretized form of diffusion Equation (29) needs to be solved at $N - 2$ ($1 < i < N$) nodes, starting from i = 2 to $i = N - 1$. Whereas at the interface, i.e., at i = 1, the boundary condition (24a) can be written in terms of ODE as

$$\frac{dc_1}{dt} = \left(\frac{k_h \overline{p}_{g0}}{\overline{c}_0}\right)\frac{dp_g}{dt} \tag{30}$$

The final node serves as a boundary and the value of concentration is known from the boundary condition (24b), therefore at $i = N$,

$$c_N = 1 \tag{31}$$

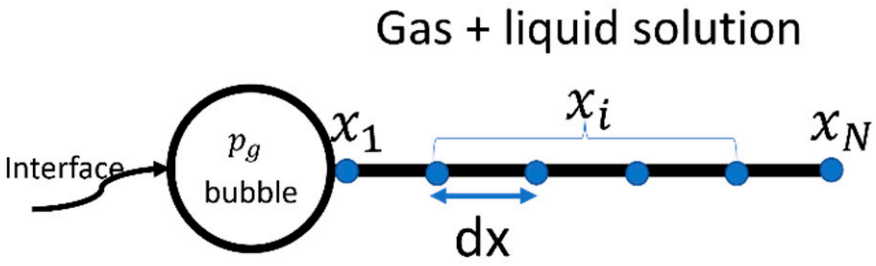


Figure 2. Numerical domain.

Similarly, the concentration gradient at the interface in Equation (21) is discretized using a forward finite difference scheme and is given as

$$\frac{\partial c}{\partial x} = \frac{c_{i+1} - c_i}{dx}, \tag{32}$$

and substituting Equation (32) in (21) results in

$$\frac{dp_g}{dt} = \frac{3I}{RPe}\left(\frac{c_{i+1} - c_i}{dx}\right) - 3\overline{p}_g\left(\frac{\dot{R}}{R}\right) \tag{33}$$

To be consistent with the notation used for the hydrodynamic ODEs (25) to (26), Equations (29) to (33) are rewritten in terms of y as follows:

For the nodes between 1 and N $(1 < i < N)$ is written as

$$\begin{aligned}\frac{dy_{3+i}}{dt} = \frac{1}{Pe}\left(\frac{2}{(x_i+y_1)}\left(\frac{y_{3+(i+1)}-y_{3+(i-1)}}{2dx}\right) + \left(\frac{y_{3+(i+1)}-2y_{3+i}+y_{3+(i-1)}}{dx^2}\right)\right)\\ -\left(\frac{y_{3+(i+1)}-y_{3+(i-1)}}{2dx}\right)\left(\frac{y_2{y_1}^2}{(x_i+y_1)^2} - y_2\right)\end{aligned} \tag{34}$$

at the interface node $(i = 1)$,

$$\frac{dc_{y_3+i}}{dt} = \frac{dy_3}{dt} \tag{35}$$

and at the final boundary node $i = N$,

$$y_{N+3} = 1. \tag{36}$$

Finally, the pressure equation takes the form:

$$\frac{dy_3}{dt} = \frac{3I}{y_1 Pe}\left(\frac{y_5 - y_4}{dx}\right) - 3y_3\left(\frac{y_2}{y_1}\right) \tag{37}$$

Therefore, the total (N +3) equations starting from (25) to (37) are the final system of ODEs that has to be solved simultaneously subjected to the initial and boundary conditions (23) to (24).

3.4. Grid Independence Test

For the numerical simulations, the infinite spatial domain is assumed to be 10 times the maximum radius of the bubble. Furthermore, the maximum radius of the bubble is anticipated to be 250 μm. This suggests that the physical infinity of the domain is 250 × 10 = 2500 μm and in terms of x_∞ it is 2250. (Note that $x = r - R(t)$). The grid independence test seeks to minimize discretization error by making the numerical solution independent of the grid

spacing. Figure 3 shows that the solution converges with increasing number of nodes. When the domain is discretized from 100 to 1000 nodes a 15% of maximum error is observed in the bubble radius and the error reduced to 2% as the number of nodes increased from 1000 to 3000; Therefore, to achieve accurate results in the numerical simulations, the domain is equally discretized with 3000 nodes.

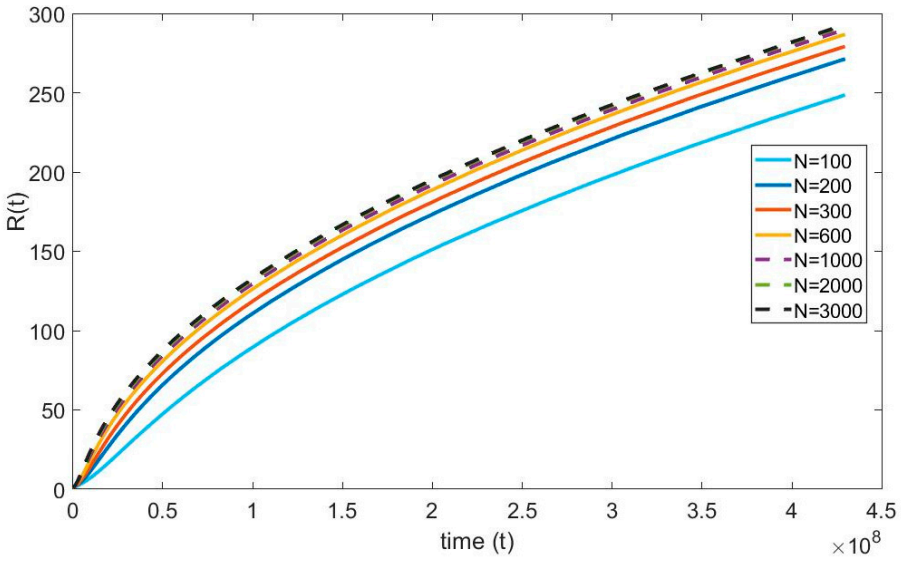


Figure 3. Grid independence test of the diffusion equation.

4. Results and Discussion

4.1. Comparison with Existing Experiments and Theory

A comparison has been made between the present model and experiment data of Han and Yoo, 1981, [17] along with the Patel, 1980, [16] and Amon and Denson, 1984, [12] models in Figure 4. The comparison is carried out based on Han and Yoo, 1981, [17] viscoelastic bubble growth experimental data for $Re = 4.5 \times 10^{-6}$, $Ca = 13.17$, $P = 1.27$, $C = 0.3$, and $Pe = 3.7 \times 10^{4}$. It is evident from the plot that the present numerical model was able to capture the experimental data more accurately than the other two models. In the initial stages, it is observed that there is a discrepancy between all the bubble growth models when compared to the experimental data of Han and Yoo, 1981, [17]. This type of divergence at the initial stage is expected, since the polymer used by Han and Yoo for the experiment exhibits the viscoelastic effect, whereas other numerical models stated in the work including the present numerical model were developed based on pure Newtonian fluid assumptions. This indicates that the viscoelastic nature of the liquid is of importance only at the initial stages and has minimum to no effects on the later stages of bubble growth.

Similarly, Figure 4 shows that the trend of the models proposed by Patel and Amon and Denson were similar at their initial and later stages. Amon and Denson's model deviates from the Patel model and moves toward the present numerical model. It is worth mentioning that the slight deviation of the aforementioned models from the present model is because of the cell model assumptions carried out by the authors in their work, whereas the present model is solved completely with the numerical approach. Overall, the present model shows more promising and accurate predictions than previous models.

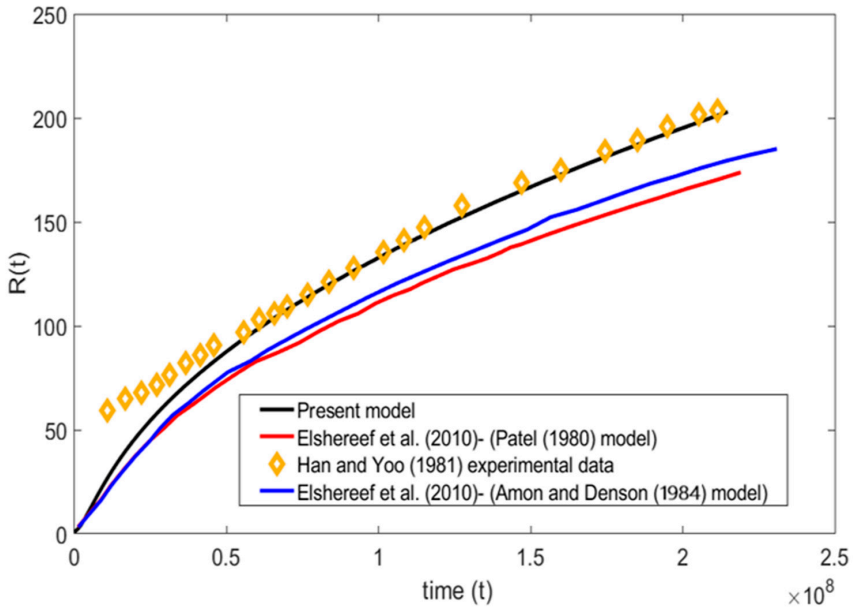


Figure 4. Present model comparison with experiment data of Han and Yoo, 1981, [17] and theory of Elshereef et al., 2010, [2], Amon and Denson, 1984, [12] and Patel, 1980, [16] ($Re = 4.5 \times 10^{-6}$, $Ca = 13.17$, $P = 1.27$, $C = 0.3$, and $Pe = 3.7 \times 10^4$).

4.2. Concentration in the Liquid

In the literature, the variation in concentration of gas in the liquid medium has not been reported or investigated thoroughly. For instance, Elshereef et al., 2010, [2] reported that his second comparison model, which is developed by Amon and Denson, 1984, [12], has solved the advection–diffusion equation using finite difference approximation. However, the concentration profiles in the liquid side were not reported. In this section, we present the concentration profile of the gas in the liquid explicitly.

Figures 5 and 6, represent the transient concentration profiles at different locations and time instances. The positional concentration profiles (Figure 5) are shown from the bubble interface, i.e., $x = 0$, to the location where the concentration gradient disappears, i.e., $x = 400$. Additionally, the time instances (Figure 6) are shown from 0.01 to 20 s. It is expected that as we move farther from the interface, the concentration gradient decreases, and this trend can be observed in Figure 5. Similarly, Figure 6 shows that at the initial time steps the concentration profile at the interface starts developing and eventually reaches a steady state with larger gradients at a larger time period.

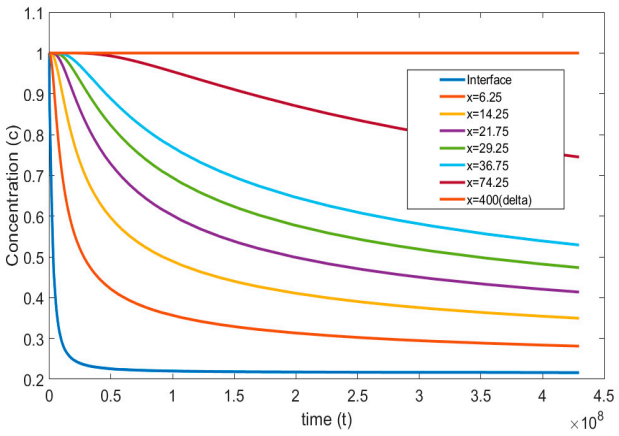


Figure 5. Concentration profiles reported at different positions with dimensionless time ($Re = 4.5 \times 10^{-6}$, $Ca = 13.17$, $P = 1.27$, $C = 0.3$, $Pe = 3.7 \times 10^4$, $t = 4.5 \times 10^8$).

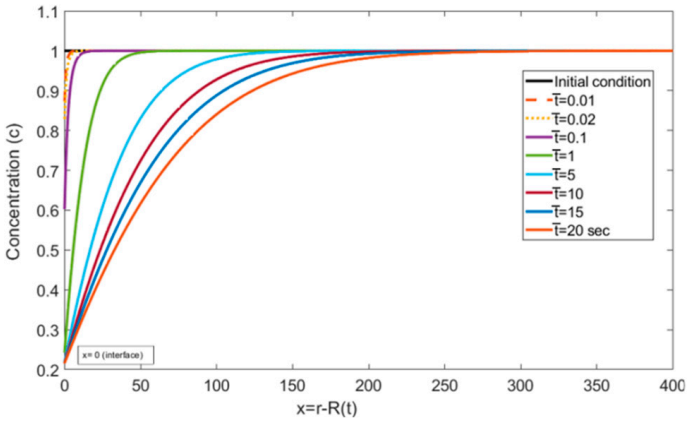


Figure 6. Concentration profiles reported in the liquid at different dimensionless time values ($Re = 4.5 \times 10^{-6}$, $Ca = 13.17$, $P = 1.27$, $C = 0.3$, and $Pe = 3.7 \times 10^{4}$).

4.3. Parametric Study of Bubble Growth

Equations (20) to (22), which constitute the full bubble growth model, emphasize that Equations (18a–c) and (19a,b), i.e., Re, Ca, Pe, P, and C, are the numbers that control bubble growth. A small change in these field parameters may affect bubble growth. In this section, an extensive study is carried out to determine the effect of these parameters on bubble growth. To do so, we only change a single parameter in non-dimensional numbers that is independent of other non-dimensional numbers. This is because if we closely observe the non-dimensional groups, they are coupled to one another by the liquid density (ρ_L), velocity ($\overline{V}$), and initial bubble radius ($\overline{R}_0$). For example, to study the effect of viscosity of the liquid, we can only change the μ_L parameter in the Reynolds number Equation (18a), and to study the effect of surface tension, we only change the σ in the capillary number Equation (18b), and so on. To observe the effects of these parameters, we need a primary or base case result to perform a relative comparison. Therefore, we consider the present numerical model results shown in Figure 4 as the primary case.

4.3.1. Effect of Viscosity on the Bubble Growth

To observe the effect of viscosity, only Reynolds number is varied, keeping other non-dimensional numbers constant. In the base case, Reynolds number is 4.5×10^{-6}, and this number is varied between 4.5×10^{-7} and 4.5×10^{-5}. In Figure 7a, at higher Reynolds numbers ($Re = 4.5 \times 10^{-5}$), the bubble growth is faster, and at lower Reynolds numbers ($Re = 4.5 \times 10^{-7}$), the bubble growth is slower. This type of behavior is expected because, at lower viscosity, the normal stress in the liquid is lower, which results in a more rapid bubble growth rate. Although the figure depicts a change in the qualitative trend with time when Re is increased, this change is only in appearance, at least initially. In fact, the slope at $t = 0$ is always zero, but the radius grows too rapidly for this to be visible; this becomes clear when we next examine the interfacial velocity.

Figure 7b shows that, if the viscosity is high, the normal stress is high, which retards bubble growth. This behavior can be well understood from Figure 7b, where the initial interface bubble velocity is high at a higher Reynolds number, suggesting rapid bubble growth. Additionally, at a lower Reynolds number, retardation of bubble interface velocity is observed, expressing that the bubble growth rate is slower. At a relatively low Re, the interfacial velocity grows slowly, reflecting a weak acceleration of the bubble, which continues to weaken with time until it vanishes, at which time the velocity reaches a maximum, reflected in the change in concavity in Figure 7a. The bubble continues to grow, but at a slower pace. This trend is similar at higher Re, but the initial growth is much faster, and the maximum is reached earlier, leading to a stronger deceleration. The change in concavity for the radius happens for any Re, but is most visible for the lowest Re shown in Figure 7a,b.

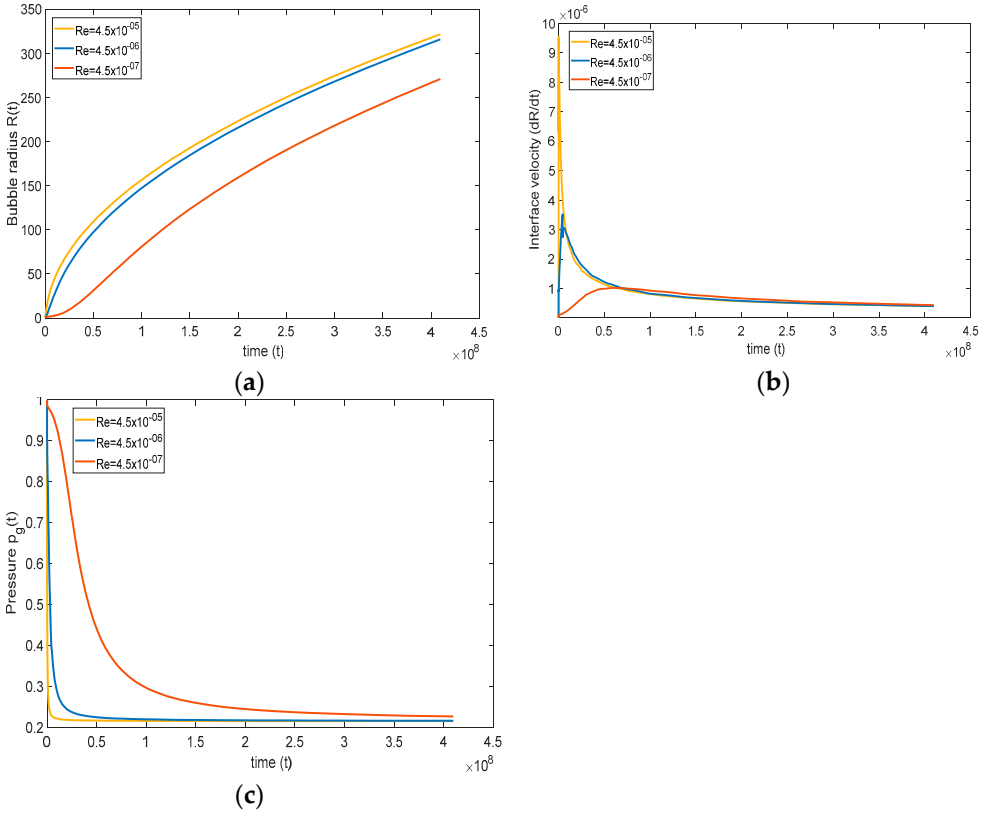


Figure 7. Effect of Reynolds number on (**a**) bubble radius, (**b**) interface velocity, and (**c**) pressure inside the gas (Ca = 13.17, P = 1.27, C = 0.3, and $Pe = 3.7 \times 10^4$).

The response in the pressure of the gas is dictated by (21), and is influenced by an intricate coupling between the evolution of the interfacial concentration gradient and the velocity. The evolution of the pressure is depicted in Figure 7c between the high and low Reynolds numbers. Typically, the pressure drops initially at a rate dominated primarily by the concentration gradient since the interface velocity is close to zero. The drop rate decreases gradually as the interface velocity increases with time. At lower Reynolds number, the pressure inside the bubble decreases slowly, reflecting a lower pressure drop, thus remaining closer to atmospheric pressure, causing slower bubble growth. On the other hand, at a high Reynolds number, the pressure inside the bubble decreases rapidly, which in turn enhances bubble growth. Finally, the maximum in the interface velocity occurs when the acceleration vanishes, and the maximum is then given by

$$\dot{R}_{\max} = -\frac{4}{3ReR} + \sqrt{\frac{16}{9Re^2R^2} + \frac{2P}{3}\Delta p - \frac{4}{3CaR}} \tag{38}$$

Clearly, the maximum vanishes if the driving pressure balances with the surface tension force. If surface tension is dominant, the maximum does not occur (see next section)

4.3.2. Effect of Surface Tension of the Liquid on the Bubble Growth

The effect of surface tension on the bubble growth is carried out with a similar approach that was demonstrated in the previous section. The capillary number is varied from the reference number while keeping other non-dimensional numbers constant. The reference capillary number is 13.17, and is varied in the range of low magnitudes Ca = 1.9 and Ca = 3. It is expected that the interfacial tension tends to retard the bubble growth by opposing the motion of the bubble boundary, and similar behavior is observed from the numerical simulations. Equation (20) clearly illustrates the competition among gas pressure, surface tension, and viscous forces on the right-hand side, as they simultaneously influence the

bubble growth. If surface tension effects are weak, then the bubble growth is dictated mainly by the gas pressure. If surface tension is increased, then the growth can be neutralized, or even reversed, as illustrated in Figure 8. The growth or collapse hinges on the initial stage, and is reflected by the initial concavity in R. If the surface tension effect is weak, then $\ddot{R}(t=0) \approx P(1-p_a) > 0$, leading to the ensuing bubble growth. On the other hand, for small Ca, $\ddot{R}(t=0) \approx -\frac{2}{Ca} < 0$, and the bubble collapses from its initial size $R(t=0) = 1$. Finally, when $Ca = \frac{2}{P(1-p_a)}$, no growth or collapse occurs.

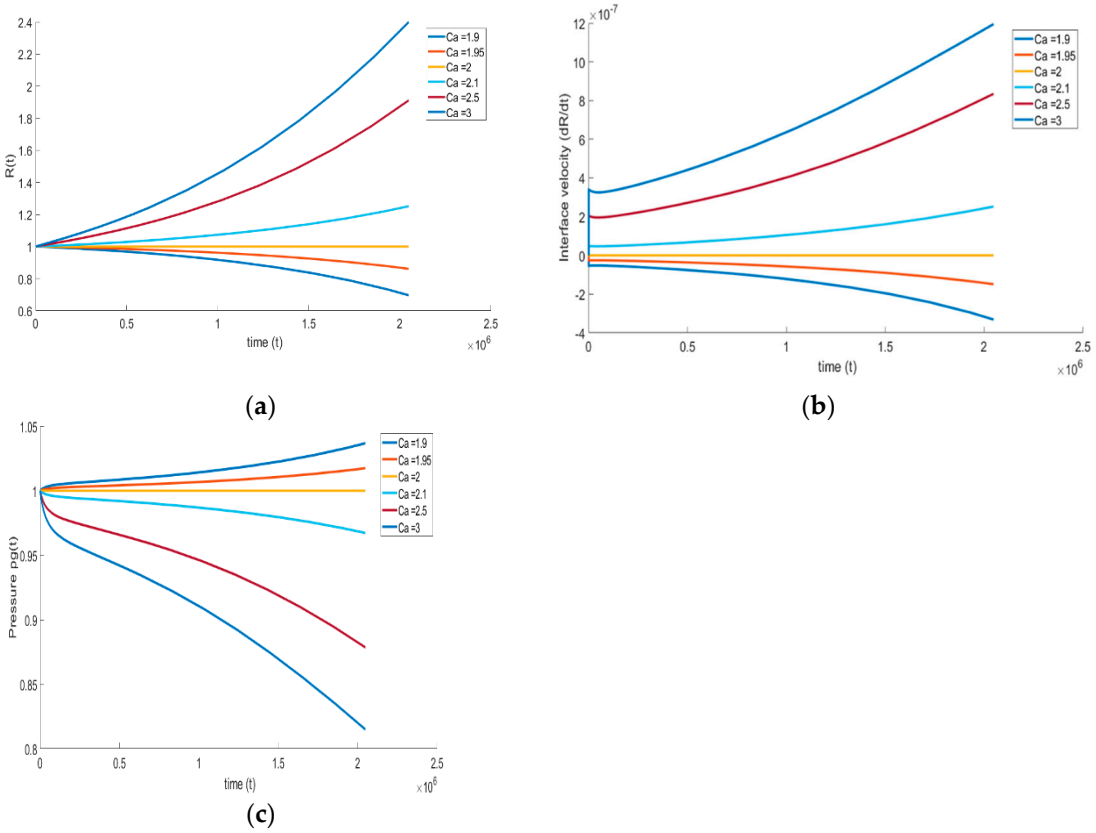


Figure 8. Effect of surface tension on (**a**) bubble growth, (**b**) interface velocity, and (**c**) pressure inside the bubble ($Re = 4.5 \times 10^{-6}$, $P = 1.27$, $C = 0.3$, and $Pe = 3.7 \times 10^4$).

We see that at approximately $Ca = 2$, the slope of the bubble growth shifts toward the positive trend, highlighting that the critical capillary number is ~2. At $Ca > 2$, the surface tension effect results in positive bubble growth. On the other hand, for $Ca < 2$ surface tension becomes dominant, and the bubble collapses. These effects can also be understood by examining the bubble interface velocity (Figure 8b) and evolution of gas pressure inside the bubble (Figure 8c). During bubble growth, the increase in interface velocity and decrease in bubble pressure is noticed; during bubble shrinkage, the decrease in interface velocity and increase in gas pressure is noticed. Finally, and as reflected in (38), we note that no maximum occurs in the interface velocity as a result of the relative dominance of surface tension.

4.3.3. Effect of Ambient Pressure on the Bubble Growth

In this section, the effect of ambient pressure (p_a) is studied. The system pressure is the ambient pressure where the growth of the bubble takes place. For instance, in the case of foaming, the system pressure is considered as the mold pressure, where the bubble growth occurs upon injecting polymer melts Han and Yoo, 1981, [17]. Similarly, in carbonated beverages, the system pressure becomes the ambient pressure.

It is important to see how the system pressure affects the overall growth of the bubble. Therefore, three cases are considered: the reference case $p_a = 0.21$ of Han and Yoo, 1981, [17], and the cases of high pressure $p_a = 0.31$ and low pressure $p_a = 0.10$. Note that the initial gas pressure (P_{g0}) in the bubble is kept constant for all the cases. One can see from Equation (20) the initial magnitude of $(p_g - p_a)$ defines the rate of bubble growth. Since the initial pressure $p_g = 1$ is the same for all the cases, and $1 > p_a$, then a higher p_a leads to a lower pressure difference and slower bubble growth, as reflected in Figure 9a–c. As the system pressure increases, bubble growth decreases, and vice versa. On decreasing the system pressure, we observe a large deviation between the base case and lower system pressure case. On the other hand, while increasing the system pressure, we observe a comparatively smaller deviation between the base case and lower system pressure case. Figure 9c indicates that the pressure drops sharply initially, at a rate that is slightly lower for higher system pressure. After the initial drop, the pressure rapidly reaches the system pressure, and bubble growth slows mainly as a result of surface tension and viscous effects.

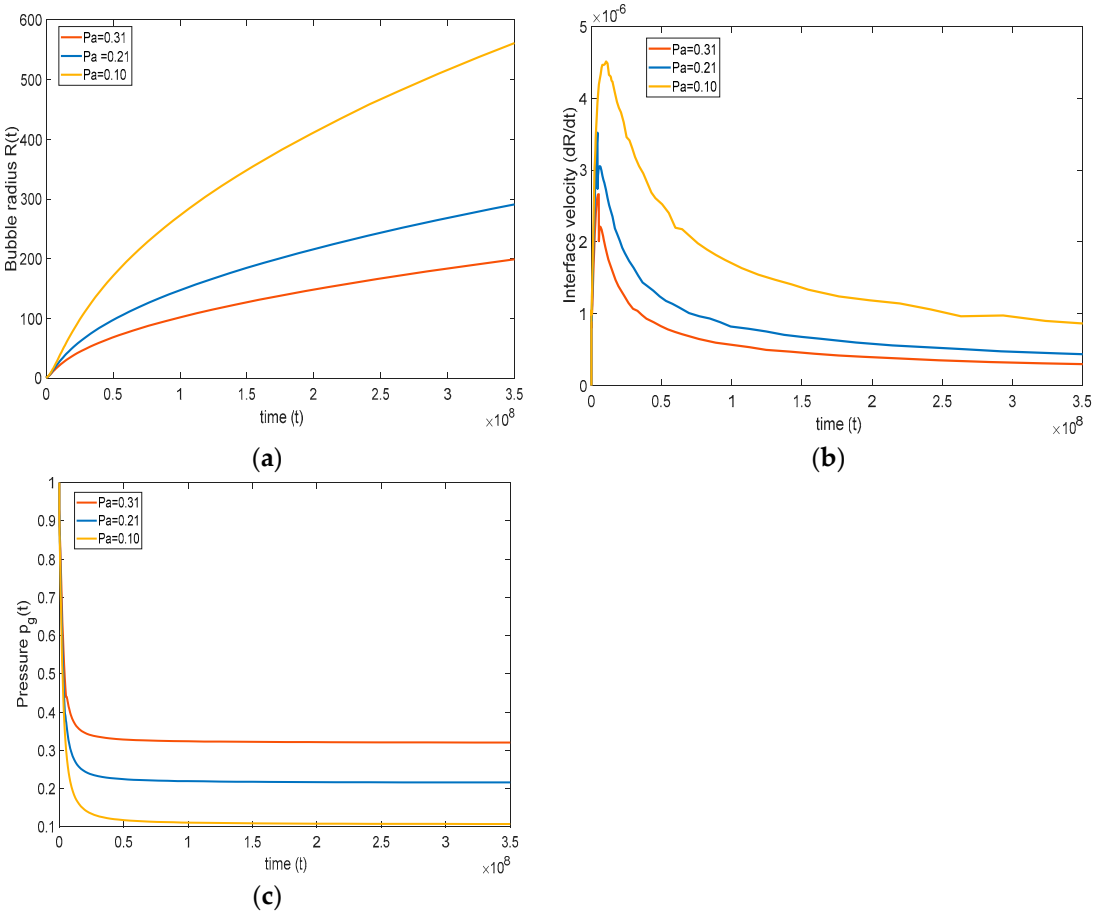


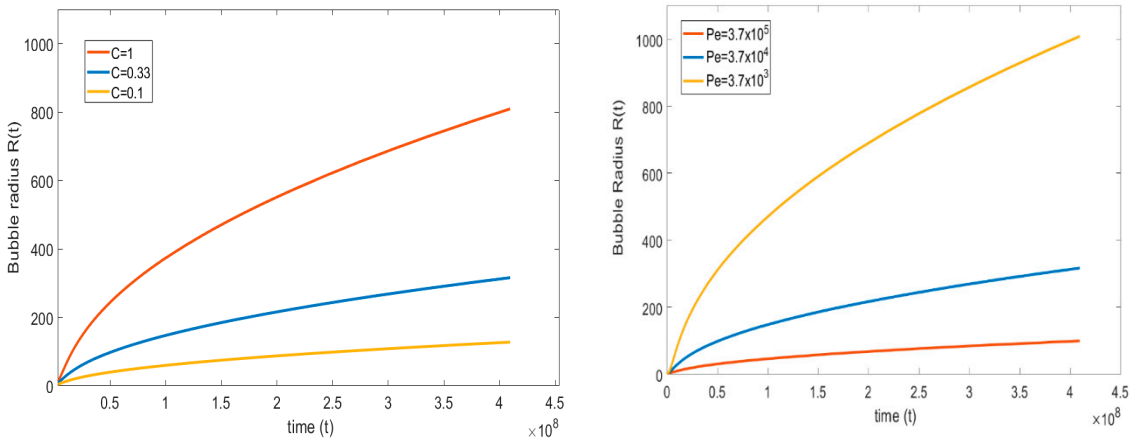
Figure 9. Effect of system pressure on (**a**) bubble growth, (**b**) interface velocity, and (**c**) pressure inside the bubble ($Re = 4.5 \times 10^{-6}$, $Ca = 13.17$, $P = 1.27$, $C = 0.3$, and $Pe = 3.7 \times 10^4$).

4.3.3.1. Effect of Solubility and Diffusion Parameters on Bubble Growth

The solubility and diffusivity of the gas in the liquid solution plays a major role in the bubble growth process. The present part focuses on studying the effect of both parameters. From the definition of Péclet number (see equation (18c)), only the diffusion coefficient is varied to maintain the other parameters as unchanged.

Therefore, a lower $Pe = 3.7 \times 10^3$ (high diffusion coefficient) and higher Péclet number $Pe = 3.7 \times 10^5$ (low diffusion coefficient) are considered. The magnitudes are compared with the base case, $Pe = 3.7 \times 10^4$. Figure 10a shows that at a lower Péclet number, the growth rate of the bubble is higher; at a higher Péclet number, the growth rate is slower.

This type of trend is predicted since, at a higher diffusion coefficient, the rate of gas flow through the interface is high, and vice versa.



(**a**) (**b**)

Figure 10. (**a**) Effect of diffusion coefficient on bubble growth; (**b**) effect of Henry's constant on bubble growth ($Re = 4.5 \times 10^{-6}$, $Ca = 13.17$, $P = 1.27$, and $C = 0.3$).

Similarly, to see the effect of solubility on bubble growth, the non-dimensional number C (see Equation (19b)), which relates to Henry's constant k_h, is varied. Here, the non-dimensional number C increases with increasing k_h and decreases by decreasing the k_h. The magnitude of the non-dimensional number C for the base case is 0.33, and this is varied between the lower number $C = 0.1$ to a higher number $C = 1$.

Figure 10b suggests that, on increasing the solubility of a gas in the liquid, the bubble growth rate is faster, and the lower the solubility of the gas in the liquid, the growth rate is lower. This result is close to physical observations; i.e., at higher solubility, the amount of gas available in the liquid is high, because the mass transfer from the liquid side to the bubble is high, resulting in a higher bubble growth rate.

5. Concluding Remarks

The hydrodynamics of a single bubble in the pool of Newtonian liquid that expands due to mass transfer was investigated in the current work. This study directly relates to foaming processes, carbonated beverages, and any other problem in which the bubble grows due to mass transfer.

Rigorous non-dimensional formulations were derived to incorporate interfacial, viscosity, diffusivity, and solubility effect on bubble growth. Especially the inertia of the liquid was included in the formulation, along with full scalar advection–diffusion processes. A strong numerical approach to the highly non-linear stiff coupled equations was discussed. The moving interface of the bubble was tackled by mapping the domain to the new coordinate (x).

The results obtained with the present formulation and numerical solution to the advection–diffusion equation was compared with the Elshereef et al., 2010, [2] models. The present numerical model predicts accurate bubble growth in comparison to Elshereef et al., 2010, [2] models. These results were validated by comparing with the Han and Yoo, 1981, [17] experimental data set.

To our knowledge, the influence and behavior of the concentration of the gas in the liquid has not been reported in the literature. In this work, a clear insight is provided on the concentration profiles of gas in the liquid and a boundary layer variation around the bubble. A simple numerical investigation was conducted to compare the variation in the approximated diffusion equation results against the present numerical results. We showed that that the gas concentration profile in the liquid deviates from the traditional concentration profile.

With the validated numerical model, a comprehensive parametric study was performed on the bubble growth. The results show that the rate of bubble growth depends primarily on the viscosity of the liquid, initial pressure difference, diffusion, and solubility. The effect of surface tension on the overall bubble growth process is limited.

We showed that the higher viscosity of the liquid lowers the bubble growth rate, and vice versa. The initial pressure difference between the bubble and the system has a significant effect on the overall bubble growth process. The higher the initial pressure difference, the greater is the bubble growth. With a lower initial pressure difference, the bubble growth is limited.

The investigation shows that the effect of diffusion and solubility of the gas in the liquid play an important role in the overall bubble growth process. Higher magnitude of these parameters leads to a higher bubble growth rate, and vice versa. It is concluded that these parameters have a similar effect on bubble growth.

Author Contributions: Conceptualization, R.K.N.M.; Methodology, R.K.N.M., R.E.K. and C.T.D.; Software, R.K.N.M.; Writing—original draft, R.K.N.M.; Writing—review and editing, R.E.K. and C.T.D. All authors have read and agreed to the published version of the manuscript.

Funding: This research received no external funding.

Institutional Review Board Statement: Not applicable.

Informed Consent Statement: Not applicable.

Data Availability Statement: Not applicable.

Conflicts of Interest: The authors declare no conflict of interest.

References

1. Rosner, D.E.; Epstein, M. Effects of interface kinetics, capillarity and solute diffusion on bubble growth rates in highly supersaturated liquids. *Chem. Eng. Sci.* **1972**, *27*, 69–88. [CrossRef]
2. Elshereef, R.; Vlachopoulos, J.; Elkamel, A. Comparison and analysis of bubble growth and foam formation models. *Eng. Comput.* **2010**, *27*, 387–408. [CrossRef]
3. Arefmanesh, A.; Advani, S.G.; Michaelides, E.E. An accurate numerical solution for mass diffusion-induced bubble growth in viscous liquids containing limited dissolved gas. *Int. J. Heat Mass Transf.* **1992**, *35*, 1711–1722. [CrossRef]
4. Lee, S.T.; Ramesh, N.S.; Campbell, G.A. Study of thermoplastic foam sheet formation. *Polym. Eng. Sci.* **1996**, *36*, 2477–2482. [CrossRef]
5. Bisperink, C.G.J.; Prins, A. Bubble growth in carbonated liquids. *Colloids Surf. A Physicochem. Eng. Asp.* **1994**, *85*, 237–253. [CrossRef]
6. Jones, S.; Evans, G.; Galvin, K. The cycle of bubble production from a gas cavity in a supersaturated solution. *Adv. Colloid Interface Sci.* **1999**, *80*, 51–84. [CrossRef]
7. Barker, G.S.; Jefferson, B.; Judd, S.J. The control of bubble size in carbonated beverages. *Chem. Eng. Sci.* **2002**, *57*, 565–573. [CrossRef]
8. Liger-Belair, G. The Physics and Chemistry behind the Bubbling Properties of Champagne and Sparkling Wines: A State-of-the-Art Review. *J. Agric. Food Chem.* **2005**, *53*, 2788–2802. [CrossRef] [PubMed]
9. Lee, W.T.; McKechnie, J.S.; Devereux, M.G. Bubble nucleation in stout beers. *Phys. Rev. E Stat. Nonlinear Soft Matter Phys.* **2011**, *83*, 1–5. [CrossRef] [PubMed]
10. Enríquez, O.R.; Hummelink, C.; Bruggert, G.-W.; Lohse, D.; Prosperetti, A.; Van Der Meer, D.; Sun, C. Growing bubbles in a slightly supersaturated liquid solution. *Rev. Sci. Instruments* **2013**, *84*, 65111. [CrossRef] [PubMed]
11. Enríquez, O.R.; Sun, C.; Lohse, D.; Prosperetti, A.; van der Meer, D. The quasi-static growth of CO2 bubbles. *J. Fluid Mech.* **2014**, *741*, 1–9. [CrossRef]
12. Amon, M.; Denson, C.D. A study of the dynamics of foam growth: Analysis of the growth of closely spaced spherical bubbles. *Polym. Eng. Sci.* **1984**, *24*, 1026–1034. [CrossRef]
13. Pooladi-Darvish, M.; Firoozabadi, A. Solution-gas drive in heavy oil reservoirs. *J. Can. Pet. Technol.* **1999**, *38*, 54–60. [CrossRef]
14. Epstein, P.S.; Plesset, M.S. On the stability of gas bubbles in liquid-gas solutions. *J. Chem. Phys.* **1950**, *18*, 1505–1509. [CrossRef]
15. Barlow, E.J.; Langlois, W.E. Diffusion of Gas from a Liquid into an Expanding Bubble. *IBM J. Res. Dev.* **1962**, *6*, 329–337. [CrossRef]
16. Patel, R.D. Bubble growth in a viscous Newtonian liquid. *Chem. Eng. Sci.* **1980**, *35*, 2352–2356. [CrossRef]
17. Han, C.D.; Yoo, H.J. Studies on structural foam processing. IV. Bubble growth during mold filling. *Polym. Eng. Sci.* **1981**, *21*, 518–533. [CrossRef]

18. Ramesh, N.S.; Rasmussen, D.H.; Campbell, G.A. Numerical and experimental studies of bubble growth during the microcellular foaming process. *Polym. Eng. Sci.* **1991**, *31*, 1657–1664. [CrossRef]
19. Soto, Á.M.; Enríquez, O.R.; Prosperetti, A.; Lohse, D.; van der Meer, D. Transition to convection in single bubble diffusive growth. *J. Fluid Mech.* **2019**, *871*, 332–349. [CrossRef]
20. Soto, M.; Lohse, D.; van der Meer, D. Diffusive growth of successive bubbles in confinement. *J. Fluid Mech.* **2020**, *882*, A6. [CrossRef]
21. Maloth, R.K.N. The Study of Bubble Growth Hydrodynamics in the Supersaturated Liquids. Master's Thesis, University of Western Ontario, London, ON, Canada, 2020.